Chemical Science

ROYAL SOCIETY OF CHEMISTRY

EDGE ARTICLE

View Article Online
View Journal | View Issue

Cite this: *Chem. Sci.*, 2024, **15**, 17435

All publication charges for this article have been paid for by the Royal Society of Chemistry

Ketone-functionalized conjugated organic polymers boost red-light-driven molecular oxygen-mediated oxygenation†

Hao Zhang, *[ab] Tingting Yuan, [a] Nursaya Zhumabay, [a] Zhipeng Ruan,*[c] Hai Qian *[b] and Magnus Rueping *[a]

Received 29th August 2024
Accepted 24th September 2024

DOI: 10.1039/d4sc05816j

rsc.li/chemical-science

Photocatalytic molecular oxygen activation has emerged as a valuable tool for organic synthesis, environmental remediation and energy conversion. Most reported instances have relied on high-energy light sources. Herein, 9-fluorenone-functionalized porous organic polymers (POPs) were reported to enable red-light-excited photocatalysis for the organic oxygenation reaction. Notably, this modification extends the conjugated backbone, allowing the capture of lower-energy light. Incorporating ketone groups into POPs also facilitates charge separation and enhances carrier concentration, thereby promoting catalytic efficiency. The new POP photomaterials exhibit high activity for the direct α-oxygenation of *N*-substituted tetrahydroisoquinolines (THIQs) using O_2 as a green oxidant under 640 nm light irradiation, achieving high yield in short reaction times. Detailed mechanistic investigations clearly showed the role of oxygen and the photocatalyst. This work provides valuable insights into the potential of ketone-modified POPs for superior photocatalytic activation of molecular oxygen under low-energy light conditions.

Introduction

Molecular oxygen is the most environmentally friendly, readily available, and cost-effective oxidant.[1–3] However, directly using molecular oxygen for organic oxidation or oxygenation under moderate conditions is challenging. A high activation barrier is required due to the spin inversion of O_2 from the triplet ground state to the high active singlet state.[4–6] Extensive research has demonstrated that photocatalysis can overcome the inherent limitations through energy transfer (EnT) or photoinduced electron transfer (PET). These processes result in the generation of reactive oxygen species (ROS) with high oxidative potential.[7–9] Photocatalytic molecular oxygen activation stands out as an important oxidation approach for processes including organic synthesis,[3] catalytic degradation of organic pollutants,[10,11] and photodynamic therapy of tumours.[12]

Several catalysts involving organic dyes, metal-based complexes, and semiconductors have been developed to use high-energy near-ultraviolet and blue light for the aerobic oxidation of organic compounds.[13–16] Our group employed a carbon nitride (CN) catalyst under blue light, achieving good yield and selectivity.[17] However, challenges persist, such as scaling up, functional group selectivity and catalyst durability.[18–22] One way to overcome the current shortcomings and limitations is by utilizing longer wavelengths of light irradiation, and photocatalysts (PCs) that are active across a broader range of the visible spectrum can enhance the efficiency of solar energy conversion.[23,24]

Typically, extensive conjugation is a characteristic feature of solar light active organic materials that exhibit broad absorption across the UV-vis to near-IR range.[25,26] Therefore, porous organic polymers (POPs) featuring large conjugated π-electron systems are ideal candidates for our goals due to their multifunctionality, robustness and non-toxicity.[27–29] POPs also possess a rigid and functionalizable backbone architecture, which enables precise tailoring of their physical and chemical properties. The Lang group introduced the sulfone group, significantly enhancing exciton separation and enabling the selective oxidation of amines under red-light irradiation.[30] Building on this work, we aim to achieve red-light-driven molecular oxygen-mediated oxygenation by incorporating specific functional sites into POPs. A critical factor influencing the PCs' effectiveness is the efficiency of intersystem crossing (ISC). A rapid and efficient ISC process leads to a greater population of excited triplet states, crucial for ROS generation.[31] In this regard, aryl ketones such as 9-fluorenone stand out for its characteristic n–π* transition, which results in a high ISC

[a]KAUST Catalysis Center, KCC, King Abdullah University of Science and Technology, KAUST, Thuwal 23955-6900, Saudi Arabia. E-mail: magnus.rueping@kaust.edu.sa

[b]Department of Chemistry, School of Science, China Pharmaceutical University, Nanjing, 211198, P. R. China. E-mail: hzhang@cpu.edu.cn; qianhai24@163.com

[c]Key Laboratory of Pharmaceutical Analysis and Laboratory Medicine (Putian University), Fujian Province University, 351100, Fujian, China. E-mail: rzp611@sina.com

† Electronic supplementary information (ESI) available. See DOI: https://doi.org/10.1039/d4sc05816j

quantum yield ($\Phi_{ISC} \approx 1$).[32–34] Xie *et al.* revealed that incorporation of ketones into the CN matrix can enhance singlet oxygen generation.[35–37] Capitalizing on the unique properties of 9-fluorenone, researchers have employed various strategies to incorporate it into different POPs. This incorporation enables the activation of molecular oxygen under high-energy light irradiation.[38–40] However, these approaches often utilize hypercrosslinked POPs or less stable imine-linked covalent organic frameworks (COFs), which inherently break extended conjugation, thereby restricting light absorption capabilities.

Pyrene is a photoactive unit with bulky π-conjugated features and broad light absorption ability. Its high planarity and abundant reaction sites provide an idea platform to polymerize small molecular PC building blocks *via* covalent linkages. The electron-rich character also makes pyrene an excellent donor unit in the skeleton of POPs.[41–45] The position of substitution significantly affects material properties, such as structural conformation and charge transport. Through a straightforward one-step cross-coupling strategy, 9-fluorenone can be attached to pyrene rings at different linkage positions, resulting in two distinct 9-fluorenone-functionalized conjugated POPs. Additionally, a reference POP was synthesized from fluorene, a structural analogue of fluorenone, to investigate the role of the ketone group. The alkynyl group serves as a conjugated connecting channel, enhancing both donor–acceptor (DA) interaction and the charge mobility of the polymers.46 The bandgap can be effectively tuned to as low as 1.75–1.87 eV, which aligns perfectly with the requirement of red light irradiation (640 nm). The POP catalysts could swell in various solvents and be easily separated for reusability and sustainability. The prepared 9-fluorenone-functionalized POPs, serving as heterogeneous PCs, can efficiently catalyze the α-oxygenation of N-substituted tetrahydroisoquinoline (THIQ) using O_2 as a green oxidant under 640 nm red-light irradiation.

Results and discussion

Material synthesis and characterization

The bottom-up strategy, combining a core-knot with linkers, is the most common approach for POP preparation.[47–49] As shown in Fig. 1a, 1,3,6,8-tetraethynylpyrene (TEP) serves as the alkynyl building block of the pyrene-based knot with D_{2h} symmetry. The different dibrominated precursors, 2,7-dibromo-9*H*-fluoren-9-one (27FO), 3,6-dibromo-9*H*-fluoren-9-one (36FO) and 2,7-dibromo-9*H*-fluorene (27FE) all share the C_2 symmetry, acting as connecting units to respectively generate three POP-based PCs labelled as **TEP-X** (X = 27FO, 36FO and 27FE). Using a mild Sonogashira–Hagihara cross-coupling method not only enables simple and efficient polymerization of the monomers, but also effectively extends the conjugated system by introducing alkyne groups. The detailed synthetic routes are provided in the ESI (Scheme S1 and S2†). The synthesized POPs are insoluble and stable in most solvents and have potential applications as heterogeneous catalysts. The representative Fourier transform infrared (FT-IR) spectra of TEP, 27FO and **TEP-27FO** are shown in Fig. 1b to confirm successful polymerization. The FT-IR spectra and analyses of **TEP-36FO** and **TEP-27FE** are respectively presented in Fig. S1 and S2.† The intense peak at 3280 cm^{-1}, previously attributed to the C–H stretching vibration of the alkynyl-terminal triple bond in TEP reactants, is not observed in the **TEP-27FO** spectrum.[50] Additionally, the characteristic C≡C stretching vibration peak has shifted from 2100 cm^{-1} to 2200 cm^{-1}, indicating the alkynyl transformation from mono-substitution in the TEP monomer into di-substitution in the **TEP-27FO** polymer.[51] The strong C–Br stretching vibration peak of the 27FO reactant at 678 cm^{-1} is also difficult to detect in the synthesized polymers. Conversely, the characteristic C=O peak of the 27FO reactant at 1716 cm^{-1} is well-preserved in **TEP-27FO**.[40] The solid-state ^{13}C nuclear magnetic resonance (^{13}C ssNMR) spectra of the samples were further analysed to verify the formation of the target polymers (Fig. 1c). The peaks at 191 ppm, not observed in **TEP-27FE**, can be assigned to the carbonyl carbons in **TEP-27FO** and **TEP-36FO**, while the characteristic 37 ppm signal of the methylene carbon in fluorene is only detectable in **TEP-27FE**. Notably, the presence of C≡C connectivity and aromatic rings in all three samples is also confirmed by the peaks at 83 ppm and the broad signal between 110 ppm and 150 ppm, respectively.[52] The surface compositions and chemical states of **TEP-X** were analysed by X-ray photoelectron spectroscopy (XPS) (Fig. S3–S5†). The survey spectrum exhibits three main peaks corresponding to O, C and Br in the polymers. No peaks corresponding to Pd and Cu are detected in any of the **TEP-X** samples owing to their trace amounts. (Table S6†) High-resolution C 1s XPS of **TEP-27FO** reveals the existence of carbon in C≡C (285.4 eV), aromatic rings (284.8 eV) and C=O (287.8 eV), consistent with the designed structure (Fig. 1d). Similar conclusions can also be drawn from the XPS spectra of other synthesized POPs. These characterization studies support the successful synthesis of the target polymers.

The morphologies of **TEP-X** were characterized by using scanning electron microscopy (SEM) and transmission electron microscopy (TEM) images, revealing an uneven and extended aggregate of layered blocks with a diameter of 2–4 μm. (Fig. S6 and S7†) Powder X-ray diffraction (PXRD) patterns and fast Fourier transform (FFT) analysis of the TEM images revealed that all the samples exhibit characteristic features of the amorphous phase, similar to that of other POPs obtained through the Sonogashira–Hagihara coupling reaction[52] (Fig. S8†). In PXRD spectra, the presence of broad peaks in the 25 to 30° range is likely due to the layered arrangement of 2D covalent sheets. Thermogravimetric (TGA) measurements revealed that all the polymers had impressive thermal stabilities owing to the existence of rigid 3D skeletons and highly cross-linked molecular structures (Fig. S9†). The 10% weight loss temperature of the materials ranged from 270 °C to 436 °C. The porosity and specific surface area of **TEP-X** were evaluated by N_2 gas sorption at 77 K (Fig. 1e). The Brunauer–Emmett–Teller (BET) surface areas were measured to be 212, 139 and 291 $m^2 g^{-1}$ for **TEP-27FO**, **TEP-36FO** and **TEP-27FE**, respectively. These differences are primarily attributed to the varying geometries of the linkers (Fig. S10†). The pore size distributions of **TEP-X** by non-local density functional theory (NLDFT) calculations were in the microporous range (0.5–2 nm), indicating the presence of

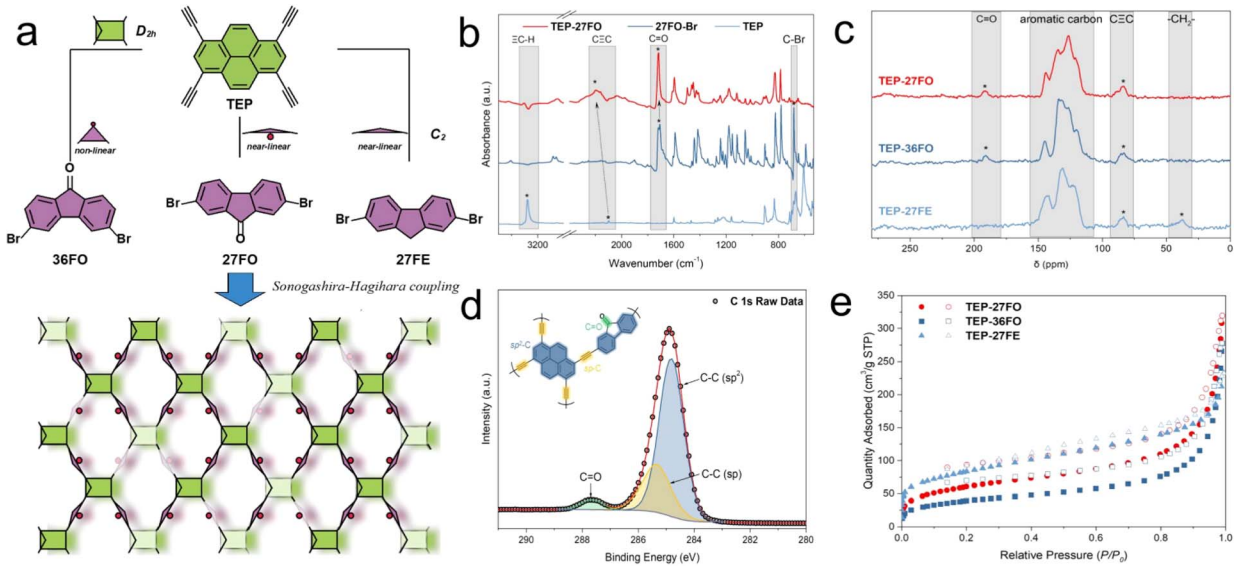

Fig. 1 (a) Synthetic procedure for **TEP-27FO**, **TEP-36FO** and **TEP-27FE**. (b) FT-IR spectra of **TEP-27FO** and its corresponding monomers. (c) ^{13}C ssNMR spectra of **TEP-X**. (d) High-resolution C 1s XPS spectra of **TEP-27FO**. (e) Nitrogen absorption–desorption isotherms of **TEP-X** at 77 K.

abundant micropores in the network (Fig. S11†). The observed low nitrogen uptake can be attributed to the increased flexibility of the amorphous POP chains. This flexibility, particularly at extremely low temperatures, allows for denser packing of the polymer. This denser packing results in poor interconnectivity of the pores, making them less accessible for nitrogen molecules. However, this behaviour is neither unexpected nor undesirable. Indeed, low-pressure adsorption/desorption hysteresis observed in the sorption curves indicates the presence of swelling effects in **TEP-X** POPs. The flexible chains of POPs can swell during catalysis at room temperature. This swelling expands the pores, facilitating access for larger substrates, which has been demonstrated by several recent studies.[53–55]

Photophysical and electrochemical investigation

Photocatalytic performance is directly linked to a material's photo-absorption characteristics, as photocatalysis relies on photo-induced generation of electron–hole pairs.[56] Consistent with this principle, we carried out UV-vis diffuse reflectance spectra (DRS) measurements, which showed broad absorption bands from the near-ultraviolet to the near-infrared region (Fig. 2a). This result indicates that red light can be efficiently captured by all **TEP-X** materials, making them promising for applications requiring red light activation. Intriguingly, all three **TEP-X** polymers exhibit a significantly extended light absorption range compared to their building block monomers. This is likely attributed to the formation of extended π-conjugated skeletons within the POP structures[57] (Fig. S12†). For example, the yellow powder of TEP and 27FO have absorption edges below 660 nm. In contrast, the deep red powder of **TEP-27FO** displayed pronounced red-shift absorption with enhanced intensity over a wide range of 200–780 nm. Tauc plots revealed the optical band gaps of **TEP-27FO**, **TEP-36FO** and **TEP-27FE** to be 1.78 eV, 1.87 eV and 1.75 eV, respectively (Fig. 2b). The experimental results seem to contradict the time-dependent density functional theory (TDDFT) calculations at the B3LYP/def2-TZVP level of theory using ORCA 5.0.4.[58] The computationally predicted trend of the model unit (M) in vertical transition is $M_{TEP\text{-}27FO} \approx M_{TEP\text{-}36FO} < M_{TEP\text{-}27FE}$ (Fig. 3). Discrepancies between theoretical predictions and experimental observations of polymers may arise from the inability of approximate model unit calculations to capture the significant structural and electronic rearrangements during polymerization.[50] The non-linear 36FO linker likely impedes efficient polymerization due to its curved binding site (Fig. 1a). This could potentially restrict the extension of π-conjugated systems, resulting in the widest optical band gap in the three polymers. In contrast, the near-linear and planar linkers of **TEP-27FO** and **TEP-27FE** are beneficial for the formation of narrower bandgaps in conjugated POPs.

However, TDDFT calculations on the model unit provide valuable insights into the electronic structures as well as visualization of the corresponding frontier molecular orbitals.[59] The optimized structures of **TEP-27FO** and **TEP-36FO** model units exhibit a clear separation of electronic states. The HOMO electron density is mainly localized on the TEP part, whereas the LUMO is delocalized across the whole model unit. This distinct spatial distribution signifies the formation of an efficient donor–acceptor pair. In contrast, different electronic distributions between the HOMO and LUMO are not evident in **TEP-27FE**. This finding suggests that the introduction of a ketone group facilitates intramolecular charge transfer (ICT) from the pyrene core-knot to the fluorenone linker.

Understanding the PCs' energy band structure is crucial because their photocatalytic activity is directly linked to the positions of the conduction band (CB) and valence band (VB), which can be determined through various techniques,

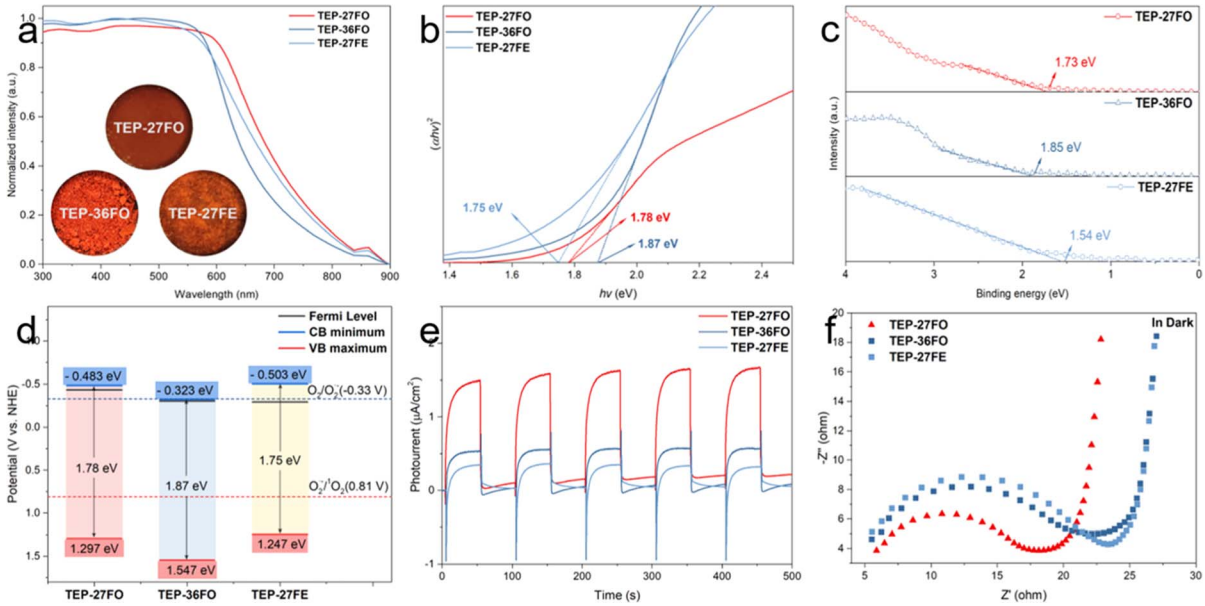

Fig. 2 (a) UV-vis DRS spectra of the TEP-X powders (inset: digital photograph). (b) Tauc plots with the band gaps. (c) VB-XPS spectra. (d) Energy band diagrams. (e) Transient photocurrent recorded under open-circuit conditions. (f) EIS Nyquist plots collected in the dark.

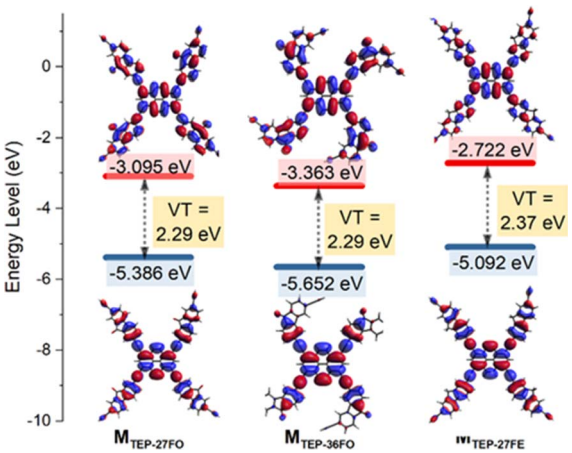

Fig. 3 The model unit of TEP-27FO, TEP-36FO, TEP-27FE named MTEP-27FO, MTEP-36FO and MTEP-27FE, respectively, and their HOMO (bottom) and LUMO (top) density plots, computed at the B3LYP/def2-TZVP level of theory using ORCA 5.0.4. Computed energies of the HOMOs and LUMOs and the vertical transitions (VT) are also provided along with each model structure.

including valence band XPS (VB-XPS) spectra, Mott–Schottky plots and UV-vis DRS spectra.[60] According to the Mott–Schottky curves, all three **TEP-X** possess a positive slope characteristic of an n-type semiconductor, while the flat-band potential (E_{fb}) of **TEP-27FO**, **TEP-36FO** and **TEP-27FE** is measured to be −0.63 V, −0.50 V and −0.49 V (*vs.* Ag/AgCl), respectively (Fig. S13†). Generally, the E_{fb} is approximately equal to the Fermi level.[61–63] And the Fermi level values *versus* the normal hydrogen electrode (*vs.* NHE) can be converted to be −0.433 V (**TEP-27FO**), −0.303 V (**TEP-36FO**) and −0.293 V (**TEP-27FE**). Meanwhile, the VB maximum positions were estimated to be 1.73 eV (**TEP-27FO**), 1.85 eV (**TEP-36FO**) and 1.54 eV (**TEP-27FE**) below the Fermi level from VB-XPS spectra (Fig. 2c).[64] Thus, the VB maximum levels *vs.* NHE were calculated to be 1.297 V (**TEP-27FO**), 1.547 V (**TEP-36FO**) and 1.247 V (**TEP-27FE**), respectively. Combining the band gaps from the above Tauc plots, we can infer that the CB minimum positions *vs.* NHE is −0.483 V (**TEP-27FO**), −0.323 V (**TEP-36FO**) and −0.503 V (**TEP-27FE**) (Fig. 2d). Considering that the standard electrode potential for reduction of O_2 to $O_2^{\bullet-}$ ($E_{red}(O_2/O_2^{\bullet-})$) is −0.33 V, the distinct CB levels in the **TEP-X** series could lead to different pathways for oxygen activation. **TEP-27FO** and **TEP-27FE** have CB levels much more negative than −0.33 V, which indicates that single electron reduction of O_2 to $O_2^{\bullet-}$ will be thermodynamically favourable. However, the more positive CB level position compared to $E_{red}(O_2/O_2^{\bullet-})$ makes **TEP-36FO** struggle to facilitate this reduction process.

The energy band diagrams of the **TEP-X** series show that their Fermi levels are situated slightly below the CB minimum and far away from the VB maximum. This observation, aligned with the positive slope of the aforementioned Mott–Schottky curves, further confirms their n-type semiconductor character. In n-type semiconductors, the electrons are the majority charge carriers, and the electron density (n) can be given by using

$$n = N_c \exp\left(-\frac{E_C - E_F}{k_B T}\right)$$

where T is the Kelvin temperature, k_B is the Boltzmann constant, N_c is the effective density of states in the CB determined by temperature T and the type of material, E_c is the CB minimum level and E_F is the Fermi level.[65,66] Obviously, a smaller difference between E_c and E_F leads to a higher electron density (n) and more efficient electron–hole separation. Compared to **TEP-27FE**, the closer proximity of the Fermi level

to the CB minimum in **TEP-27FO** and **TEP-36FO** promotes superior separation of photogenerated electron–hole pairs. This may be because the ketone group increases the donor density to fill surface states located below the CB edge, effectively increasing carrier mobility and lifetime.[67] The charge transfer ability of the **TEP-X** series is further supported by electron paramagnetic resonance (EPR) spectroscopy, photo-current spectra and electrochemical impedance spectroscopy (EIS) measurements. The EPR spectra of **TEP-X** powders show a single Lorenztian-line with $g = 2.003$, assigned to the unpaired electrons of the ketone group in the delocalized π-state system[68] (Fig. S14†). After 15 min red-light (>600 nm) irradiation, the signal of all three samples exhibits varying degrees of enhancement, implying that electrons are excited from the VB to the CB, forming electron–hole pairs. Among them **TEP-27FO** shows the strongest enhancement, indicating that it possesses the greatest electron density and the best photogenerated electron–hole separation efficiency. Meanwhile, transient photocurrent response (*i*–*t*) curves demonstrated that the three **TEP-X** PCs maintain good reproducibility of the response intensity across switching cycles. The photocurrent intensities followed the order: **TEP-27FE** < **TEP-36FO** < **TEP-27FO**. The highest transient photocurrent density was observed for **TEP-27FO**, suggesting that the incorporation of well-ordered 9-fluorenone significantly promotes carrier separation and migration within the photocatalyst skeleton (Fig. 2e). In the Nyquist plot of EIS, **TEP-27FO** exhibited the smallest radius of the semicircle under both light-on and light-off conditions (Fig. 2f and S15†). The lower charge transfer resistance of **TEP-27FO** signifies its superior charge separation rate for electron–hole pairs. With its suitable red-light-absorbing bandgap, favourable oxygen activation potential, and superior charge separation capability, **TEP-27FO** as a photocatalyst holds great promise for efficient red light-driven oxygen activation.

Photocatalytic performance

Numerous natural products, synthetic analogs, and bioactive mimetics incorporating the 1,2,3,4-tetrahydroisoquinoline (THIQ) scaffold have been reported with significant antiviral, antifungal, antibacterial, antidiabetic, and antineoplastic activities. Direct α-oxygenation of the THIQ core efficiently generates 3,4-dihydroisoquinolones, providing a valuable and efficient tool for accessing diverse structural scaffolds with pharmaceutical potential[69–71] (Fig. S16†). The Zhang group developed ketone-based COF PCs to facilitate this oxidation process under white light irradiation.[39] Therefore, we adopted this model reaction to validate the concept of red-light-driven molecular oxygen-mediated oxygenation. Initial optimization experiments identified the prepared **TEP-X** PCs as particularly effective for the red-light-driven direct α-oxygenation of the THIQ core. The reaction utilized 2-(4-methoxyphenyl)-1,2,3,4-tetrahydroisoquinoline (**1a**) as the model substrate, 1,5-diazabicyclo[4.3.0]non-5-ene (DBN) as the base, molecular oxygen as the oxidant, and acetonitrile (MeCN) as the solvent under 640 nm red light irradiation. Consistent with the predictions of the optoelectronic characterization, **TEP-27FO** exhibited the best catalytic performance, achieving a high isolated yield of 94% in 2 hours. In contrast, **TEP-36FO** and **TEP-27FE** required a longer reaction time of 12 h to achieve a comparable high yield (Table 1, entry 1–3 and Table S1,† entry 1–2). Employing their building monomer 9-fluorenone, fluorene and TEP as the catalyst resulted in negligible product formation under red light irradiation, suggesting the significance of a large π-conjugated skeleton within **TEP-X** PCs for efficient red-light absorption during the catalytic process (Table 1, entry 4–6). Control experiments evidenced that the photocatalyst, base, light, and oxygen are indispensable for this reaction (Table 1, entries 7–10). No product was formed when the reaction was conducted at 60 °C without light, indicating that the process is photochemical rather than thermal (Table 1, entry 11). Additionally, the product yield significantly decreased when the reaction was carried out under open air conditions (Table 1, entry 12). Detailed optimization studies, including screening of different bases, solvents and light are given in the ESI† (Tables S2–S4†).

As **TEP-27FO** has a high photocatalytic efficiency in direct α-oxygenation of THIQ, we performed trapping experiments to gain mechanistic insight. First, $CuCl_2$ and triethanolamine (TEOA) almost completely inhibited the oxidation reaction, indicating the important roles of the electrons and holes produced by photoexcitation. Afterwards, three ROS scavengers, benoquinone (BQ) for $O_2^{\bullet-}$, *t*-butanol for $^{\bullet}OH$ and NaN_3 for $^1O_2$, were added to verify the active species of the oxidation process. The yields were also dramatically decreased when the superoxide radical ($O_2^{\bullet-}$) was quenched with BQ. In contrast, the reaction could proceed smoothly when *t*-butanol and NaN_3 were present, implying that hydroxyl radicals ($^{\bullet}OH$) and singlet

Table 1 Optimization and control reactions[a]

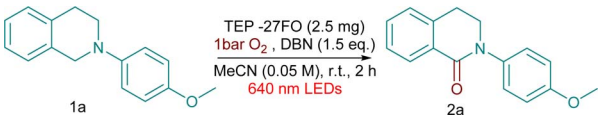

Entry	Deviation from the above	Yield (%)[b]
1	None	94[c]
2	**TEP-36FO** as the catalyst	26
3	**TEP-27FE** as the catalyst	43
4	9-Fluorenone as the catalyst	ND
5	Fluorene as the catalyst	ND
6	TEP as the catalyst	Trace
7	No catalyst	ND
8	No light	ND
9	No base	ND
10	Argon instead of O_2	ND
11	At 60 °C (dark)	ND
12	Open air	18

[a] Standard conditions: 0.1 mmol of the substrate, 2.5 mg of **TEP-27FO** as the catalyst, 1.5 equiv. of DBN, 2 mL of MeCN (0.05 M), 640 nm Kessil LED lamp (40 W) with fan cooling, room temperature (25–30 °C), 2 hours. [b] GC yield using *n*-dodecane as the internal standard. [c] Isolated yield. "ND" means not detected.

oxygen ($^1O_2$) have almost no influence on the reaction (Fig. 4a and Table S1,† entry 3–9). 2,2,6,6-Tetramethylpiperidine-1-oxyl (TEMPO) and butylated hydroxytoluene (BHT), typically known to quench radicals, surprisingly exhibit minimal impact on the catalytic process, unlike many observed oxygen activation reactions[16,72,73] (Table S1,† entry 3–4). Meanwhile, high resolution mass spectrometry (HRMS) analysis of the reaction mixture also suggested the absence of potentially generated TEMPO-captured or BHT-captured THIQ radicals. These results, coupled with TEMPO's ability to act as a hydrogen atom transfer (HAT) agent, indicates that free radicals might not be the main intermediates in this reaction.[74,75] In addition, *in situ* electron paramagnetic resonance (EPR) measurements were carried out to detect the formation of the spin reactive species. 5,5-dimethyl-1-pyrroline-*N*-oxide (DMPO) and 2,2,6,6-tetramethyl piperidine (TEMP) are employed as $O_2^{\bullet-}$ and $^1O_2$ trapping agents, respectively. In line with expectations, the characteristic peak signals for DMPO-$O_2^{\bullet-}$ and TEMP-$^1O_2$ exhibited a certain degree of enhancement following red light irradiation of the **TEP-27FO** suspension, confirming the efficacy of **TEP-27FO** in activating molecular oxygen to produce $O_2^{\bullet-}$ and $^1O_2$. Noteworthily, the addition of the reaction substrate THIQ **1a** to the *in situ* EPR system caused a prominent enhancement in the characteristic peak signal of DMPO-$O_2^{\bullet-}$, which was approximately seven times stronger than that observed in the absence of the substrate. In contrast, a similar operation led to a diminution of the TEMP-$^1O_2$ characteristic peak signal (Fig. 4b and c). This finding suggests an interaction between **TEP-27FO** and the reaction substrate THIQ **1a**, leading to a substantial enhancement in the generation of $O_2^{\bullet-}$ while suppressing the formation of $^1O_2$. We guess that $O_2^{\bullet-}$ and $^1O_2$ could originate from separate competing pathways. We also investigated the potential role of trace metal impurities like Pd and Cu as active sites in the studied reaction, which were introduced during the synthesis of **TPE-X**. The combination of acid washing and Soxhlet extraction proved to be an effective post-treatment method for minimizing Pd and Cu residues in the samples.[52] Inductively coupled plasma optical emission spectroscopy (ICP-OES) was employed to determine that only trace amounts (ppm level) of transition metals were detected (Table S6†). Furthermore, the addition of $Pd(Ph_3P)_2Cl_2$ and CuI to the standard reaction significantly inhibited the catalytic process (Table S1,† entry 10–11). Trace metal impurities are very unlikely to exert a strong catalytic influence on the reaction.

Under standard conditions, gas chromatography mass spectrometry (GC-MS) analysis of the reaction solution after 0.5 hours revealed the presence of a key imide cation intermediate, 2-(4-methoxyphenyl)-3,4-dihydroisoquinolin-2-ium (Fig. S17†). Upon screening acetone as the reaction solvent, trace amounts of the byproduct 1-(2-(4-methoxyphenyl)-1,2,3,4-tetrahydroisoquinolin-1-yl)propan-2-one (**2aa**) were detected, indicating a cross-dehydrogenative coupling (CDC) reaction between *N*-aryl substituted THIQ and acetone. Interestingly, adding a catalytic amount of L-proline promoted the transformation of **2aa** into the main product, achieving a remarkable isolated yield of 83% (Table S5, Fig. S18 and S19†). L-Proline is well-known for its ability to catalyze the formation of nucleophilic enamines from ketones, which can then attack THIQ imide cation intermediates to generate the product **2aa** (Fig. S20†). This result indirectly confirms the existence of a key imide cation intermediate.[76] Based on the detailed mechanistic experiment and previous report,[72,73,77,78] we propose the following catalytic cycle as described in Fig. 4d. First, a ketone-modified POP, acting as a photosensitizer (PS), is excited under red light irradiation to generate an excited state species (PS*). PS* can activate molecular oxygen through two competing pathways: photo-induced electron transfer (PET) and energy transfer (EnT). The $^1O_2$ species typically arises from the EnT

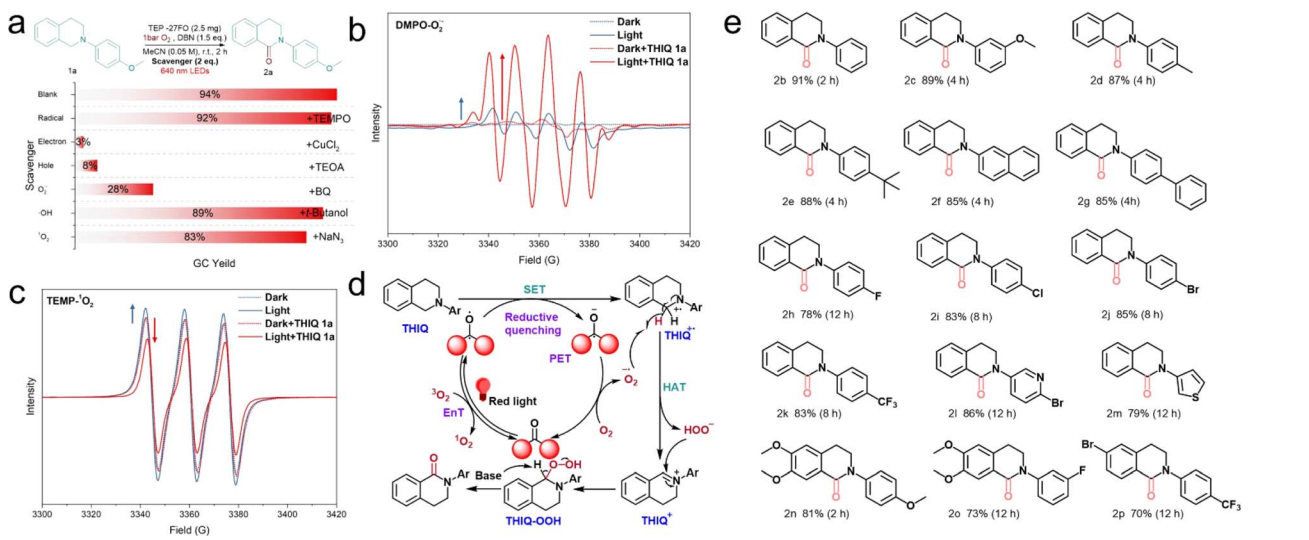

Fig. 4 (a) Active species trapping experiments for mechanistic studies. (b) *In situ* ESR spectra of DMPO-$O_2^{\bullet-}$ for **TEP-27FO** and its TIHQ **1a** mixture in the dark and under 15 min of red-light irradiation (>600 nm). (c) *In situ* ESR spectra of TEMPO-$^1O_2$ for **TEP-27FO** and its TIHQ **1a** mixture in the dark and under 15 min of red-light irradiation (>600 nm). (d) Proposed catalytic mechanism. (e) Substrate scope for photocatalytic direct α-oxygenation of THIQ derivatives under standard conditions.

process between PS* and triplet oxygen. In the PET process, a single electron transfer (SET) from the THIQ substrate to PS* initiates reductive quenching to obtain a radical anion $PS^{\bullet -}$ and aminyl cation radical $THIQ^{\bullet +}$. Following a redox reaction between oxygen and $PS^{\bullet -}$, a superoxide radical anion ($O_2^{\bullet -}$) is formed. This key ROS species then facilitates the HAT process from $THIQ^{\bullet +}$, leading to the formation of the key imide cation intermediate ($THIQ^+$) and hydroperoxide anion (HOO^-). Finally, the nucleophilic HOO^- undergoes an addition reaction with $THIQ^+$ to form hydroperoxide intermediate THIQ–OOH, which could provide the desired product through a proton abstraction by using a base. The PET process involves two consecutive SET steps with a THIQ substrate as the electron donor (D) and O_2 as the electron acceptor (A).[23] Upon the addition of a THIQ substrate, the excited triplet state of **TEP-27FO** preferentially undergoes the PET pathway for $O_2^{\bullet -}$ generation, rather than the EnT pathway for $^1O_2$ formation. This is consistent with the EPR experimental result previously mentioned.

To evaluate the reusability and stability of **TEP-27FO** as a heterogeneous PC, we subjected it to repeated catalytic cycles. Notably, the catalytic activity remained largely unchanged after at least five cycles (Fig. S21†). Furthermore, characterization techniques like FT-IR and UV-vis spectroscopy revealed minimal alterations in the composition and functionality of **TEP-27FO** before and after the repeated reactions (Fig. S22 and S23†). **TEP-27FO** is also stable and robust in acidic and basic solutions and common organic solvents for long-term photocatalytic cycling processes (Fig. S24†). Encouraged by **TEP-27FO**'s exceptional efficiency and sustainability as PCs for red-light-driven molecular oxygen-mediated oxygenation, we also investigated the substrate scope of dihydroisoquinolone synthesis to further demonstrate its broad applicability (Fig. 4e). Notably, the reaction was tolerant to various *N*-substituted THIQs as shown in Table S7.† The desired α-oxygenation products were obtained in moderate to high yields (70–94%) in less than 12 h. Various N-aryl substituted THIQs provided the desired dihydroisoquinolones in the presence of both electron-donating (–OMe, –Me, –butyl, and –phenyl) and electron-withdrawing (–F, –Cl, –Br, and $–CF_3$) substituents. The electron-rich THIQ derivatives presented higher reaction rates compared to those of electron-deficient ones. Specifically, longer reaction times were required for fluoro and trifluoromethyl substituents. Furthermore, this method could be applied to the heterocyclic substituted THIQ with good yield. We also observed that steric hindrance did not significantly impact the yield of the corresponding products. Introducing the substituents (–OMe and –Br) on the THIQ aryl ring resulted in a modest reduction in yield.

Conclusions

In summary, our study demonstrates that incorporating a 9-fluorenone unit into conjugated POPs significantly enhances good performance in direct α-oxygenation of THIQ *via* red-light-driven molecular oxygen activation. The modular design strategy effectively combines the unique advantages of both aryl ketones and POPs: a 9-fluorenone unit serves as the catalytic centre, effectively activating oxygen to form $O_2^{\bullet -}$ through the PET process, while the large conjugated feature of POPs lowers the bandgap, enabling the absorption of low-energy light. Additionally, the ability of POPs to swell in various solvents provides them with excellent reusability and sustainability, overcoming the solubility challenge faced by homogeneous catalysts. These promising results highlight the potential for developing high-performance organic photocatalysts that leverage aryl ketones as the core scaffold for mild and sustainable red-light-driven molecular oxygen activation.

Data availability

The data supporting this article have been included as part of the ESI.†

Author contributions

H. Z., Z. R., H. Q. and M. R. conceived of the idea. H. Z. performed the experiments and the data analysis. T. Y. carried out the catalytic testing and analyzed the data. N. Z. conducted the SEM and ICP-OES tests and analyzed the data. H. Z. and M. R. co-wrote the manuscript. all authors discussed and edited the manuscript.

Conflicts of interest

The authors declare no competing financial interest.

Acknowledgements

H. Zhang acknowledges the China Scholarship Council (CSC) for the support (202207060017). This study was supported by the National Natural Science Foundation of China (Project No. 21703288) and the Open Project Program (PLAM 202204) of Key Laboratory of Pharmaceutical Analysis and Laboratory Medicine (Putian University).

Notes and references

1 Q. Li and F. Li, *Chem. Eng. J.*, 2021, **421**, 129915.
2 A. N. Campbell and S. S. Stahl, *Acc. Chem. Res.*, 2012, **45**, 851–863.
3 C. Tang, X. Qiu, Z. Cheng and N. Jiao, *Chem. Soc. Rev.*, 2021, **50**, 8067–8101.
4 Y. Zheng, Z. Yu, H. Ou, A. M. Asiri, Y. Chen and X. Wang, *Adv. Funct. Mater.*, 2018, **28**, 1705407.
5 A. U. Khan, *J. Phys. Chem.*, 1976, **80**, 2219–2228.
6 R. Long, K. Mao, X. Ye, W. Yan, Y. Huang, J. Wang, Y. Fu, X. Wang, X. Wu, Y. Xie and Y. Xiong, *J. Am. Chem. Soc.*, 2013, **135**, 3200–3207.
7 L. Marzo, S. K. Pagire, O. Reiser and B. König, *Angew. Chem., Int. Ed.*, 2018, **57**, 10034–10072.
8 S. Ma, J.-W. Cui, C.-H. Rao, M.-Z. Jia, Y.-R. Chen and J. Zhang, *Green Chem.*, 2021, **23**, 1337–1343.

9 Y. Zhang, D. Riemer, W. Schilling, J. Kollmann and S. Das, *ACS Catal.*, 2018, **8**, 6659–6664.
10 L. Zhou, Y. Liu, H. Shi, Y. Qing, C. Chen, L. Shen, M. Zhou, B. Li and H. Lin, *Water Res.*, 2024, **250**, 121075.
11 Z.-H. Xie, C.-S. He, D.-N. Pei, Y. Dong, S.-R. Yang, Z. Xiong, P. Zhou, Z.-C. Pan, G. Yao and B. Lai, *Chem. Eng. J.*, 2023, **468**, 143778.
12 D. E. J. G. J. Dolmans, D. Fukumura and R. K. Jain, *Nat. Rev. Cancer*, 2003, **3**, 380–387.
13 Y. Qian, D. Li, Y. Han and H.-L. Jiang, *J. Am. Chem. Soc.*, 2020, **142**, 20763–20771.
14 P. Geng, Y. Tang, G. Pan, W. Wang, J. Hu and Y. Cai, *Green Chem.*, 2019, **21**, 6116–6122.
15 Y. Zhang, W. Schilling, D. Riemer and S. Das, *Nat. Protoc.*, 2020, **15**, 822–839.
16 S.-S. Zhu, Y. Liu, X.-L. Chen, L.-B. Qu and B. Yu, *ACS Catal.*, 2022, **12**, 126–134.
17 K. Murugesan, A. Sagadevan, L. Peng, O. Savateev and M. Rueping, *ACS Catal.*, 2023, **13**, 13414–13422.
18 S. L. Goldschmid, N. E. Soon Tay, C. L. Joe, B. C. Lainhart, T. C. Sherwood, E. M. Simmons, M. Sezen-Edmonds and T. Rovis, *J. Am. Chem. Soc.*, 2022, **144**, 22409–22415.
19 N. Sellet, M. Cormier and J.-P. Goddard, *Org. Chem. Front.*, 2021, **8**, 6783–6790.
20 Z. Deng, H. Li, S. Chen, N. Wang, G. Liu, D. Liu, W. Ou, F. Xu, X. Wang, D. Lei, P.-C. Lo, Y. Y. Li, J. Lu, M. Yang, M.-L. He and G. Zhu, *Nat. Chem.*, 2023, **15**, 930–939.
21 B. D. Ravetz, N. E. S. Tay, C. L. Joe, M. Sezen-Edmonds, M. A. Schmidt, Y. Tan, J. M. Janey, M. D. Eastgate and T. Rovis, *ACS Cent. Sci.*, 2020, **6**, 2053–2059.
22 F. Calogero, G. Magagnano, S. Potenti, F. Pasca, A. Fermi, A. Gualandi, P. Ceroni, G. Bergamini and P. G. Cozzi, *Chem. Sci.*, 2022, **13**, 5973–5981.
23 A. H. Schade and L. Mei, *Org. Biomol. Chem.*, 2023, **21**, 2472–2485.
24 P. Yang, R. Wang, M. Zhou and X. Wang, *Angew. Chem., Int. Ed.*, 2018, **57**, 8674–8677.
25 F. Vilela, K. Zhang and M. Antonietti, *Energy Environ. Sci.*, 2012, **5**, 7819.
26 L. Yang, Y. Peng, X. Luo, Y. Dan, J. Ye, Y. Zhou and Z. Zou, *Chem. Soc. Rev.*, 2021, **50**, 2147–2172.
27 T. Banerjee, F. Podjaski, J. Kröger, B. P. Biswal and B. V. Lotsch, *Nat. Rev. Mater.*, 2020, **6**, 168–190.
28 J.-S. M. Lee and A. I. Cooper, *Chem. Rev.*, 2020, **120**, 2171–2214.
29 Z. Zhang, J. Jia, Y. Zhi, S. Ma and X. Liu, *Chem. Soc. Rev.*, 2022, **51**, 2444–2490.
30 X. Dong, F. Zhang, F. Huang and X. Lang, *Appl. Catal., B*, 2022, **318**, 121875.
31 S. Suleman, Y. Zhang, Y. Qian, J. Zhang, Z. Lin, Ö. Metin, Z. Meng and H. Jiang, *Angew. Chem., Int. Ed.*, 2024, **63**, e202314988.
32 F. Strieth-Kalthoff and F. Glorius, *Chem*, 2020, **6**, 1888–1903.
33 A. Davison, M. J. S. Dewar, K. Hafner, E. Heilbronner, U. Hofmann, J.-M. Lehn, K. Niedenzu, K. Schäfer, G. Wittig, F. L. Boschke and P. J. Wagner, in *Triplet States III*, Springer Berlin Heidelberg, Berlin, Heidelberg, 1976, vol. 66, pp. 1–52.
34 Y. Su, X. Du, B. Fu, G. Wang, X. Piao, G. Wang and K. Zhang, *ACS Mater. Lett.*, 2024, **6**, 1042–1049.
35 H. Wang, S. Jiang, S. Chen, D. Li, X. Zhang, W. Shao, X. Sun, J. Xie, Z. Zhao, Q. Zhang, Y. Tian and Y. Xie, *Adv. Mater.*, 2016, **28**, 6940–6945.
36 H. Wang, S. Jiang, W. Liu, X. Zhang, Q. Zhang, Y. Luo and Y. Xie, *Angew. Chem., Int. Ed.*, 2020, **59**, 11093–11100.
37 W. Liu, H. Che, B. Liu and Y. Ao, *J. Mater. Chem. A*, 2024, **12**, 13427–13434.
38 Y. Zhi, K. Li, H. Xia, M. Xue, Y. Mu and X. Liu, *J. Mater. Chem. A*, 2017, **5**, 8697–8704.
39 M. Liu, J. Liu, J. Li, Z. Zhao, K. Zhou, Y. Li, P. He, J. Wu, Z. Bao, Q. Yang, Y. Yang, Q. Ren and Z. Zhang, *J. Am. Chem. Soc.*, 2023, **145**, 9198–9206.
40 Y. Wang, X. Feng, J. Cao, X. Zheng, X. Gong, W. Yu, M. Wang and S. Shi, *Angew. Chem., Int. Ed.*, 2024, e202319139.
41 X. Dong, H. Zhao, K. Zhang and X. Lang, *Coord. Chem. Rev.*, 2024, **513**, 215902.
42 Y. Fan, D. W. Kang, S. Labalme, J. Li and W. Lin, *Angew. Chem., Int. Ed.*, 2023, **62**, e202218908.
43 J. Sun, H. Sekhar Jena, C. Krishnaraj, K. Singh Rawat, S. Abednatanzi, J. Chakraborty, A. Laemont, W. Liu, H. Chen, Y. Liu, K. Leus, H. Vrielinck, V. Van Speybroeck and P. Van Der Voort, *Angew. Chem., Int. Ed.*, 2023, **62**, e202216719.
44 X. Li, Y. Wang, F. Zhang and X. Lang, *Appl. Catal., B*, 2024, **340**, 123190.
45 R. Bu, L. Zhang, X.-Y. Liu, S.-L. Yang, G. Li and E.-Q. Gao, *ACS Appl. Mater. Interfaces*, 2021, **13**, 26431–26440.
46 S. Wang, X. Hai, X. Ding, S. Jin, Y. Xiang, P. Wang, B. Jiang, F. Ichihara, M. Oshikiri, X. Meng, Y. Li, W. Matsuda, J. Ma, S. Seki, X. Wang, H. Huang, Y. Wada, H. Chen and J. Ye, *Nat. Commun.*, 2020, **11**, 1149.
47 S. Das, P. Heasman, T. Ben and S. Qiu, *Chem. Rev.*, 2017, **117**, 1515–1563.
48 T. Zhang, G. Xing, W. Chen and L. Chen, *Mater. Chem. Front.*, 2020, **4**, 332–353.
49 M. G. Mohamed, A. F. M. EL-Mahdy, M. G. Kotp and S.-W. Kuo, *Adv. Mater.*, 2022, **3**, 707–733.
50 X. Yu, Z. Yang, B. Qiu, S. Guo, P. Yang, B. Yu, H. Zhang, Y. Zhao, X. Yang, B. Han and Z. Liu, *Angew. Chem., Int. Ed.*, 2019, **58**, 632–636.
51 Y. Cao, H. Fang, C. Guo, W. Sun, Y. Xu, Y. Wu and Y. Wang, *Angew. Chem., Int. Ed.*, 2023, **62**, e202302143.
52 N. Yin, W. Chen, Y. Yang, Z. Tang, P. Li, X. Zhang, L. Tang, T. Wang, Y. Wang, Y. Zhou and Z. Zou, *Chin. J. Catal.*, 2023, **51**, 168–179.
53 A. R. Antonangelo, N. Hawkins, E. Tocci, C. Muzzi, A. Fuoco and M. Carta, *J. Am. Chem. Soc.*, 2022, **144**, 15581–15594.
54 R. T. Woodward, L. A. Stevens, R. Dawson, M. Vijayaraghavan, T. Hasell, I. P. Silverwood, A. V. Ewing, T. Ratvijitvech, J. D. Exley, S. Y. Chong, F. Blanc, D. J. Adams, S. G. Kazarian, C. E. Snape, T. C. Drage and A. I. Cooper, *J. Am. Chem. Soc.*, 2014, **136**, 9028–9035.
55 J. Jeromenok and J. Weber, *Langmuir*, 2013, **29**, 12982–12989.

56 G. Zhao, H. Pang, G. Liu, P. Li, H. Liu, H. Zhang, L. Shi and J. Ye, *Appl. Catal., B*, 2017, **200**, 141–149.
57 J. Kosco, F. Moruzzi, B. Willner and I. McCulloch, *Adv. Energy Mater.*, 2020, **10**, 2001935.
58 F. Neese, *Wiley Interdiscip. Rev.: Comput. Mol. Sci.*, 2022, **12**, e1606.
59 S. Barman, A. Singh, F. A. Rahimi and T. K. Maji, *J. Am. Chem. Soc.*, 2021, **143**, 16284–16292.
60 D. Xu, S.-N. Zhang, J.-S. Chen and X.-H. Li, *Chem. Rev.*, 2023, **123**, 1–30.
61 X. Li, B. Kang, F. Dong, Z. Zhang, X. Luo, L. Han, J. Huang, Z. Feng, Z. Chen, J. Xu, B. Peng and Z. L. Wang, *Nano Energy*, 2021, **81**, 105671.
62 N. Tian, Y. Zhang, X. Li, K. Xiao, X. Du, F. Dong, G. I. N. Waterhouse, T. Zhang and H. Huang, *Nano Energy*, 2017, **38**, 72–81.
63 Y. Yu, P. Zhang, Y. Kuang, Y. Ding, J. Yao, J. Xu and Y. Cao, *J. Phys. Chem. C*, 2014, **118**, 20982–20988.
64 D. Jiang, X. Sun, X. Wu, S. Zhang, X. Qu, L. Shi, Y. Zhang and F. Du, *Nanophotonics*, 2020, **9**, 2077–2088.
65 S. M. Sze and K. K. Ng, *Physics of semiconductor devices*, Wiley-Interscience, Hoboken, N.J, 3rd edn, 2007.
66 K. M. Van Vliet and A. H. Marshak, *Phys. Status Solidi B*, 1980, **101**, 525–530.
67 C. Fàbrega, D. Monllor-Satoca, S. Ampudia, A. Parra, T. Andreu and J. R. Morante, *J. Phys. Chem. C*, 2013, **117**, 20517–20524.
68 D. Dvoranová, Z. Barbieriková, M. Mazúr, E. I. García-López, G. Marcì, K. Lušpai and V. Brezová, *J. Photochem. Photobiol., A*, 2019, **375**, 100–113.
69 N. Palmer, T. M. Peakman, D. Norton and D. C. Rees, *Org. Biomol. Chem.*, 2016, **14**, 1599–1610.
70 J. Li, H. Wang, H. Jin, Z. Xiang, L. Chen, P. J. Walsh and G. Liang, *Org. Lett.*, 2022, **24**, 8125–8129.
71 Y. Zhang, D. Riemer, W. Schilling, J. Kollmann and S. Das, *ACS Catal.*, 2018, **8**, 6659–6664.
72 K. C. C. Aganda, B. Hong and A. Lee, *Adv. Synth. Catal.*, 2019, **361**, 1124–1129.
73 Y. Zhang, D. Riemer, W. Schilling, J. Kollmann and S. Das, *ACS Catal.*, 2018, **8**, 6659–6664.
74 J. W. Lee, S. Lim, D. N. Maienshein, P. Liu and M. Ngai, *Angew. Chem., Int. Ed.*, 2020, **59**, 21475–21480.
75 T. Ito, F. W. Seidel, X. Jin and K. Nozaki, *J. Org. Chem.*, 2022, **87**, 12733–12740.
76 G. Kumar, S. R. Dash and S. Neogi, *J. Catal.*, 2021, **394**, 40–49.
77 Y. Bai, Q. Yang, Y. Tang, X. Dan, W. Wang and Y. Cai, *Green Chem.*, 2023, **25**, 4446–4452.
78 H. Bartling, A. Eisenhofer, B. König and R. M. Gschwind, *J. Am. Chem. Soc.*, 2016, **138**, 11860–11871.